

Article

The Late Carboniferous Mafic–Ultramafic Complex Induced by Slab Breakoff in Eastern North Tianshan, Central Asian Orogenic Belt

Feng Gao ^{1,2,*} , Yuanfeng Cheng ^{1,2}, Ruiqing Guo ^{1,2}, Xiaoqiang Liu ^{1,2} and Zengxin Liu ^{1,2}

¹ Xinjiang Key Laboratory for Geodynamic Processes and Metallogenic Prognosis of the Central Asian Orogenic Belt, Urumqi 830046, China; chengyuanfeng@xju.edu.cn (Y.C.); guoruiqing8888@163.com (R.G.); xiaoqliu2011@163.com (X.L.); 18061147785@163.com (Z.L.)

² School of Geology and Mining Engineering, Xinjiang University, Urumqi 830046, China

* Correspondence: gaof@xju.edu.cn; Tel.: +86-17699918038

Abstract: The Late Carboniferous to Early Permian is a critical period of the Chinese Tianshan, witnessing the tectonic transition from subduction to post-collisional extension during the final amalgamation of the Central Asian Orogenic Belt (CAOB). The late Carboniferous Mozbaysay mafic–ultramafic complex in the Qijiaoqing–Balikun area, eastern North Tianshan, provides important clues for revealing the nature and timing of this tectonic transition. The Mozbaysay complex comprises mainly hornblende gabbros and lherzolites. LA-ICP-MS U–Pb zircon ages of hornblende gabbro yielded a weighted mean age of 306 ± 1.9 Ma for this complex. These mafic–ultramafic rocks have high contents of MgO (up to 30 wt.%), Cr (up to 2493 ppm), and Ni (up to 1041 ppm), but low contents of SiO₂ (40.34–47.70 wt.%). They are enriched in LREE and show characteristics of enriched mid-ocean ridge basalts (E-MORB). The relatively high Th/Yb and Ba/Nb ratios imply the mantle sources could have been metasomatized by slab–mantle interaction with aqueous fluids from dehydration of the subducted slab. Thus, these mafic–ultramafic rocks were most likely produced by partial melting of the asthenospheric and lithospheric mantle with a slight influence of slab-derived fluids. Therefore, we suggest that the formation of these Late Carboniferous mafic–ultramafic rocks was triggered by the decompression-induced influx of asthenospheric heat and melting through a slab window during post-collisional slab breakoff. Combined with geological data, the petrogenetic links of the Late Carboniferous mafic–ultramafic rocks in eastern North Tianshan to slab breakoff suggest that the tectonic transition from convergence to post-collision most likely initiated in situ at ca. 306 Ma and lasted to ca. 300 Ma.

Keywords: mafic–ultramafic rocks; Central Asian Orogenic Belt; asthenosphere–lithosphere interaction; slab breakoff



Citation: Gao, F.; Cheng, Y.; Guo, R.; Liu, X.; Liu, Z. The Late Carboniferous Mafic–Ultramafic Complex Induced by Slab Breakoff in Eastern North Tianshan, Central Asian Orogenic Belt. *Minerals* **2023**, *13*, 1293. <https://doi.org/10.3390/min13101293>

Academic Editor: Giorgio Garuti

Received: 30 August 2023

Revised: 29 September 2023

Accepted: 30 September 2023

Published: 4 October 2023



Copyright: © 2023 by the authors. Licensee MDPI, Basel, Switzerland. This article is an open access article distributed under the terms and conditions of the Creative Commons Attribution (CC BY) license (<https://creativecommons.org/licenses/by/4.0/>).

1. Introduction

The Central Asian Orogenic Belt (CAOB) or Altaids is the largest Phanerozoic (ca. 1.0–0.25 Ga) accretionary system on Earth [1–4]. The Chinese Tianshan lies in the southmost part of CAOB and records the final amalgamation of the Kazakhstan and Tuva–Mongol reclines, as well as the collision of the Tarim and North China cratons (Figure 1; [1,2,4]). The Late Carboniferous to Early Permian was thought to be a crucial period in the evolutionary history of the Chinese Tianshan, marked by the closure of the paleo-Tianshan Ocean, the transition from subduction/accretion to post-collisional extension tectonism and the occurrence of extensive mantle-derived magmatism [4–7]. However, the nature and timing of this tectonic transition remain open questions.

Mafic–ultramafic rocks as mantle-derived magmas can be generated in various tectonic settings. In-depth analysis of mantle source compositions, physicochemical conditions for source partial melting, and magmatic processes of non-ophiolitic mafic–ultramafic

could provide crucial insights into understanding the tectonic setting in which they were generated and further unraveling the tectonic evolutionary history of ancient orogenic belts [8–15]. Significant volumes of Late Carboniferous to Early Permian mafic–ultramafic rocks intruded in the eastern North Tianshan tectonic belt (NTB). Many of these complexes exhibit Ni-Cu-(PGE) sulfide mineralization (Figure 1b; [7,13,16,17]). Although previous studies have investigated their ages, petrogenesis, tectonic settings, and mineralization mechanisms [13,18–20], the geodynamic setting of these mafic–ultramafic rocks remains controversial. Some researchers have proposed that they were generated by either oblique subduction or ridge subduction [10,13,18,21–23]. Others have attributed the formation of these mafic–ultramafic complexes to magmatism induced by slab breakoff in a syn- or post-collisional tectonic setting [16,17,24–28]. Furthermore, some researchers also argued that these mafic–ultramafic magmas were generated in a continental rift setting associated with a mantle plume [10,29–31]. Therefore, determining the ages and tectonic setting of these mafic–ultramafic complexes is of key importance for understanding the nature and timing of the tectonic transition of eastern NTB and the general role they played in the geodynamic processes of accretionary orogenesis during the Late Carboniferous to Early Permian period.

In this contribution, geochronological and geochemical analyses were conducted on the Mozbaysay mafic–ultramafic complex located in the Qijiaoqing–Balikun region, eastern NTB (Figure 2). In combination with available geological data, we attempt to (1) determine the age and isotopic characteristics of the studied mafic–ultramafic rocks to constrain their formation age and magma source characteristics, (2) understand the role of slab–mantle interaction in mantle metasomatism, and (3) shed light on the tectonic transition mechanism and timing in eastern NTB during the Late Carboniferous to Early Permian period.

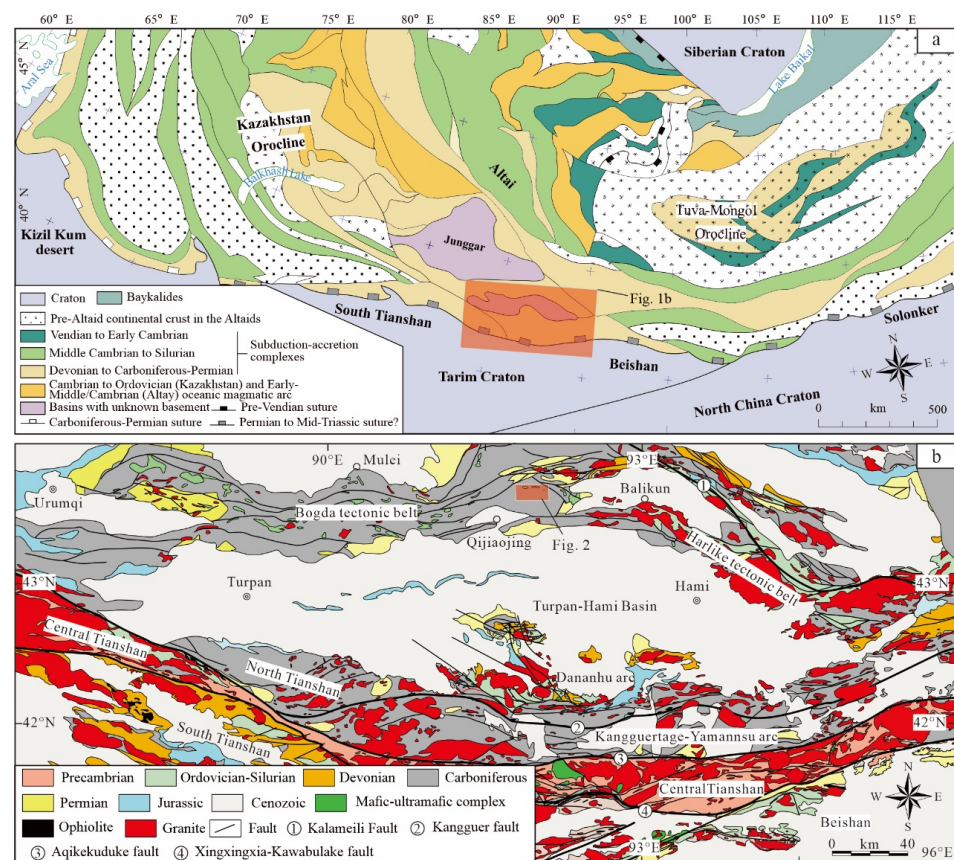


Figure 1. (a) Simplified tectonic map of the Central Asian Orogenic Belt, modified from Jahn et al. [32]. (b) Geological map of the Chinese eastern North Tianshan and adjacent areas, modified from Xiao et al. [21].

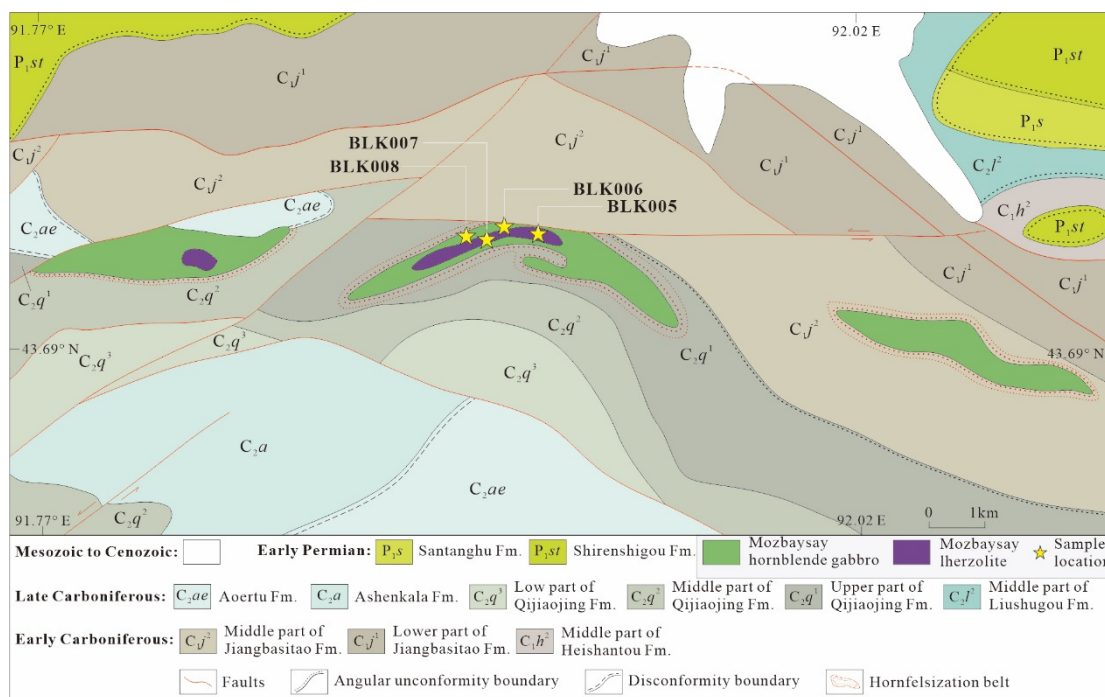


Figure 2. Geological map of the study area in the Qijiaoqing–Balikun region with sample locations (modified after Sandaoling Geological Map at 1:200,000 scale [33]).

2. Regional Geology

The Chinese segment of the Tianshan orogenic belt in the south CAOB can be geographically divided into eastern and western parts along the Urumqi–Korla highway. The Eastern Chinese Tianshan can be further divided into three tectonic units as the North Tianshan, Central Tianshan, and South Tianshan tectonic belts from north to south (Figure 1; [6,21]). The North Tianshan tectonic belt (NTB) in the following text refers to the NTB in the East Tianshan. The NTB is predominantly composed of Ordovician to Carboniferous volcano-sedimentary sequences crosscut by Paleozoic granitoids [34]. Generally, it is considered a Paleozoic arc system formed by the southward subduction of the Kalamaili Ocean, and/or northward subduction of the North Tianshan Ocean [7,16,21,35–37]. This belt can be further divided into three subunits, i.e., the Bogda–Harlik, Dananhu, and Kangguer–Yamansu tectonic belts that are unconformably covered by the Mesozoic–Cenozoic Turpan–Hami Basin (Figure 1b; [21,34]). Numerous Late Carboniferous to Early Permian mafic–ultramafic complexes are distributed in these tectonic domains (Figure 1b). They are generally along subparallel trans-lithospheric faults bounding tectonic units or subunits, and many of them bear Ni–Cu–(PGE) sulfide ores [13,17,19].

3. Outcrop and Petrography

The Mozbaysay mafic–ultramafic complex is exposed in the Qijiaoqing–Balikun area in the northeast margin of the Turpan Hami basin, NTB (Figure 2), is a component of the Late Carboniferous to Early Permian mantle-derived magmatic rock belt around the Turpan basin [38]. This complex consists of three individual bodies of different sizes, which are spatially distributed in a nearly east–west direction (Figure 2). The country rocks of this complex are volcano-sedimentary rocks of the Early Carboniferous Jiangbasitao Formation (C_{1j}) and Late Carboniferous Qijiaoqing Formation (C_{2q}) (Figure 2). The intrusive boundary is characterized by a hornfelsization belt (Figure 2). In addition, these complexes display a ring-shaped feature in space. The outer zone mainly consists of grayish-black to grayish-green hornblende gabbros, with an exposure width of 100–500 m and 1 km at most. The core part is composed of grayish-black lherzolites, with a short axis of 300–400 m and a long axis of more than 3 km. These two rock types are in transitional contact

without obvious boundaries (Figures 2 and 3). Banded rhythmic structures can be seen at the margin of the Iherzolite plutons, with a spacing of approximately 4 cm (Figure 3c). The characteristics mentioned above may suggest the emplacement of en-echelon intrusions formed by deformation and diapir-like upward expulsion of a layered complex.

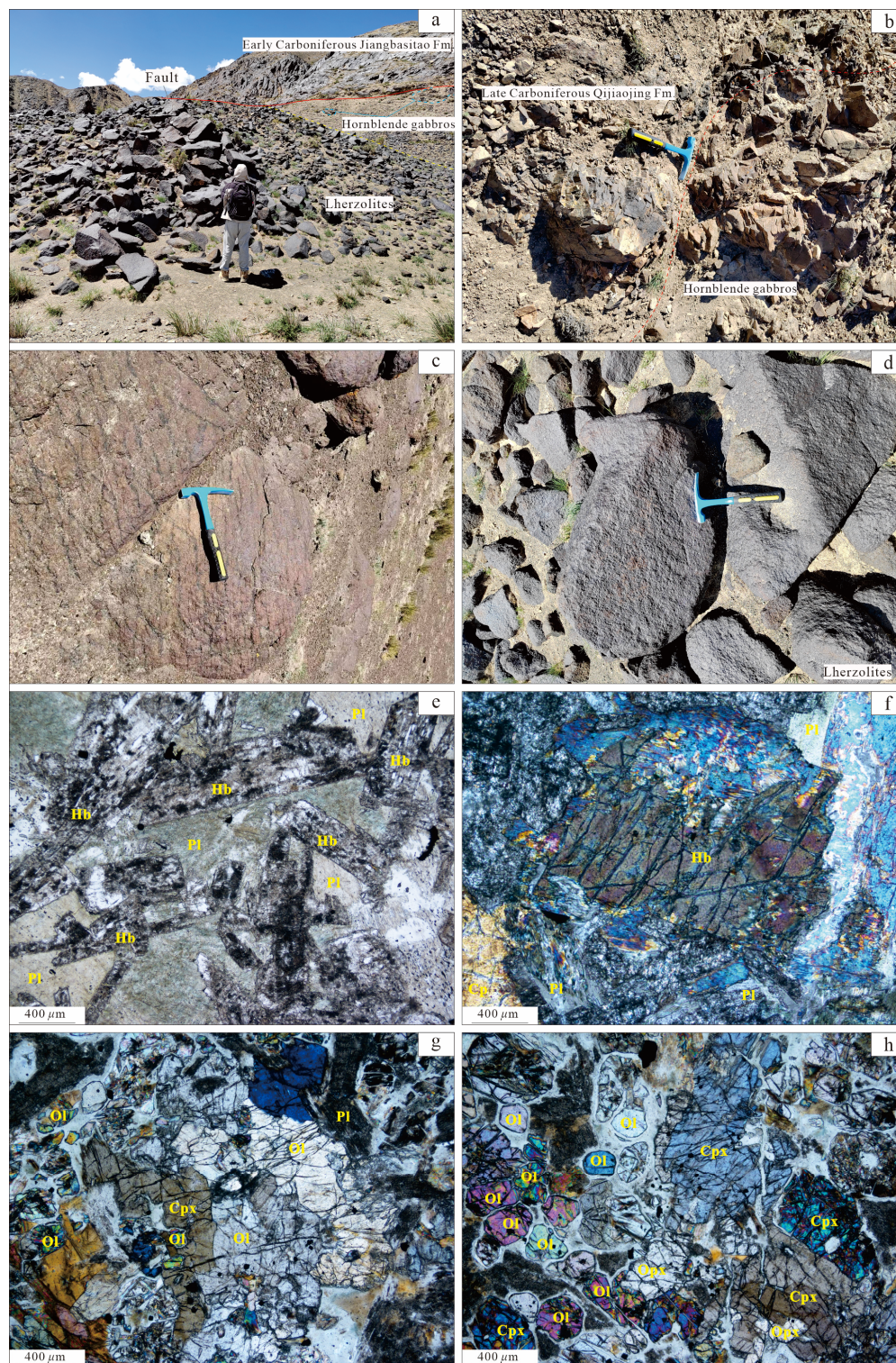


Figure 3. Representative field (a–d) and microscopic (e–h, under cross-polarized light) photos of the Mozbaysay hornblende gabbros and Iherzolites in the Balikun area, eastern North Tianshan. Abbreviations: Ol—olivine; Opx—orthopyroxene; Cpx—clinopyroxene; Pl—plagioclase; Hb—hornblende.

The hornblende gabbro is composed of plagioclase (40–45%), hornblende (35–40%), and accessory phases (5–10%) including phlogopite, apatite, and magnetite (Figure 3e,f). Plagioclase crystals are commonly euhedral and medium- to fine-grained, lath-shaped with well-developed twinning, and some have been replaced by sericite. Hornblende crystals are commonly euhedral to subhedral, medium- to fine-grained, and are interstitial to plagioclase (Figure 3e,f). Hornblende crystals often display destabilization rims composed of biotite and chlorite (Figure 3e,f). The lherzolite displays a poikilitic texture and contains 50–55% olivine, 15–20% clinopyroxene, 10–15% orthopyroxene, and a trace amount of plagioclase, hornblende, and magnetite (5–10%). Olivine crystals are commonly euhedral to subhedral, fine- to medium-grained, and are mostly altered to iddingsite and serpentine (Figure 3g,h). Clinopyroxene and orthopyroxene form large intergranular crystals along the boundaries of olivine crystals (Figure 3g,h).

4. Analytical Results

4.1. Zircon U-Pb Dating

One hornblende gabbro sample (BLK008TW1) was selected for zircon U-Pb dating. The detailed zircon U-Pb dating results are summarized in Table S1 and shown in Figure 4. Zircons from the hornblende gabbro are transparent, stubby and subhedral, 50–150 μm in size, with length/width ratios of 1:1–3:1, and clear zoning in CL images (Figure 4a). Fourteen zircons were analyzed, and their Th and U contents, and the Th/U values of these of these zircons are 273–3761 ppm, 238–2098 ppm, and 0.80–3.66 (Figure 4b), respectively, indicating magmatic origins. Nineteen zircon analyses from the hornblende gabbro sample yield $^{206}\text{Pb}/^{238}\text{U}$ ages of 305–307 Ma, with a weighted mean age of 305.7 ± 1.9 Ma (MSWD = 0.013; Figure 4a), which we interpret to be the crystallization age of the hornblende gabbro. Zircons with older $^{206}\text{Pb}/^{238}\text{U}$ ages are interpreted to be xenocrysts incorporated from the wall rocks. In addition, as the hornblende gabbro and lherzolite are spatially associated, and show a gradual transitional relationship without obvious boundary, we hence infer that they formed nearly simultaneously at ca. 306 Ma.

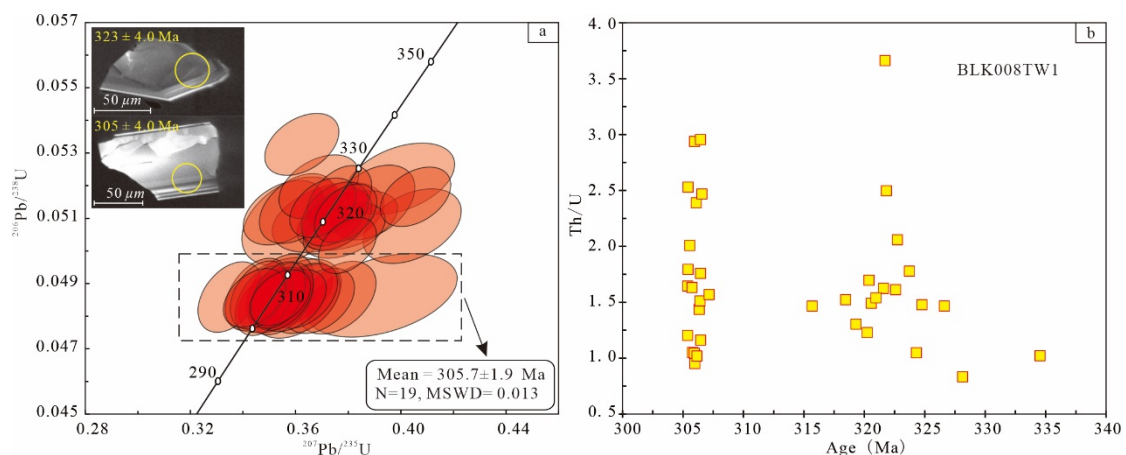


Figure 4. (a) Laser ablation–inductively coupled plasma–mass spectrometry (LA-ICP-MS) zircon U-Pb Concordia diagrams for the Mozbaysay hornblende gabbro and (b) Th/U versus age diagram of zircons for the hornblende gabbro. MSWD—mean square of weighted deviates.

4.2. Whole-Rock Major and Trace Elements

A total of twenty samples, including ten lherzolite samples and ten hornblende gabbro samples from the Mozbaysay complex were prepared for whole-rock major and trace element analysis, and the results are listed in Table S2.

The lherzolites from Mozbaysay with SiO_2 contents of 40.34–44.02 wt.% and MgO contents of 24.89–30.33 wt.% (Table S2). Their Na_2O and K_2O contents ranged from 0.20 wt.% to 0.61 wt.% and from 0.38 wt.% to 0.88 wt.%, respectively. They have relatively constant contents of Al_2O_3

(6.23–10.58 wt.%), $\text{Fe}_2\text{O}_3^{\text{T}}$ (13.84–16.92 wt.%), CaO (3.33–5.90 wt.%), TiO_2 (0.51–0.61 wt.%), and MgO (24.89–30.33 wt.%; $\text{Mg}^{\#} = 75.78\text{--}76.92$). These samples possess high Cr (1394–2493 ppm) and Ni (722–1041 ppm) but low total rare earth element (REE) (28.34–38.18 ppm) concentrations. The hornblende gabbros from Mozbaysay are with relatively high contents of SiO_2 (44.11–47.70 wt.%), Na_2O (1.96–3.65 wt.%), and K_2O (0.23–1.98 wt.%) but low contents of MgO (7.68–10.98 wt.%, $\text{Mg}^{\#} = 59.82\text{--}72.54$). These samples possess relatively low Cr (165–408 ppm) and Ni (66.60–247.00 ppm) and high total REE (33.76–80.12 ppm) concentrations.

In the chondrite-normalized REE diagram (Figure 5a), all Mozbaysay mafic–ultramafic rocks exhibit slight light rare earth element (LREE) enrichment with $(\text{La}/\text{Yb})_{\text{N}} = 2.13\text{--}4.87$. The hornblende gabbros have slightly positive Eu anomalies ($\text{Eu}/\text{Eu}^* = 1.09\text{--}1.94$), while the lherzolites have slightly negative Eu anomalies ($\text{Eu}/\text{Eu}^* = 0.71\text{--}0.97$). In the primitive mantle-normalized trace element spidergram (Figure 5b), they are characterized by enrichment of large-ion lithophile elements (LILE, e.g., Rb, Ba, and K) but depletion of Th, U, Nb, and Ta.

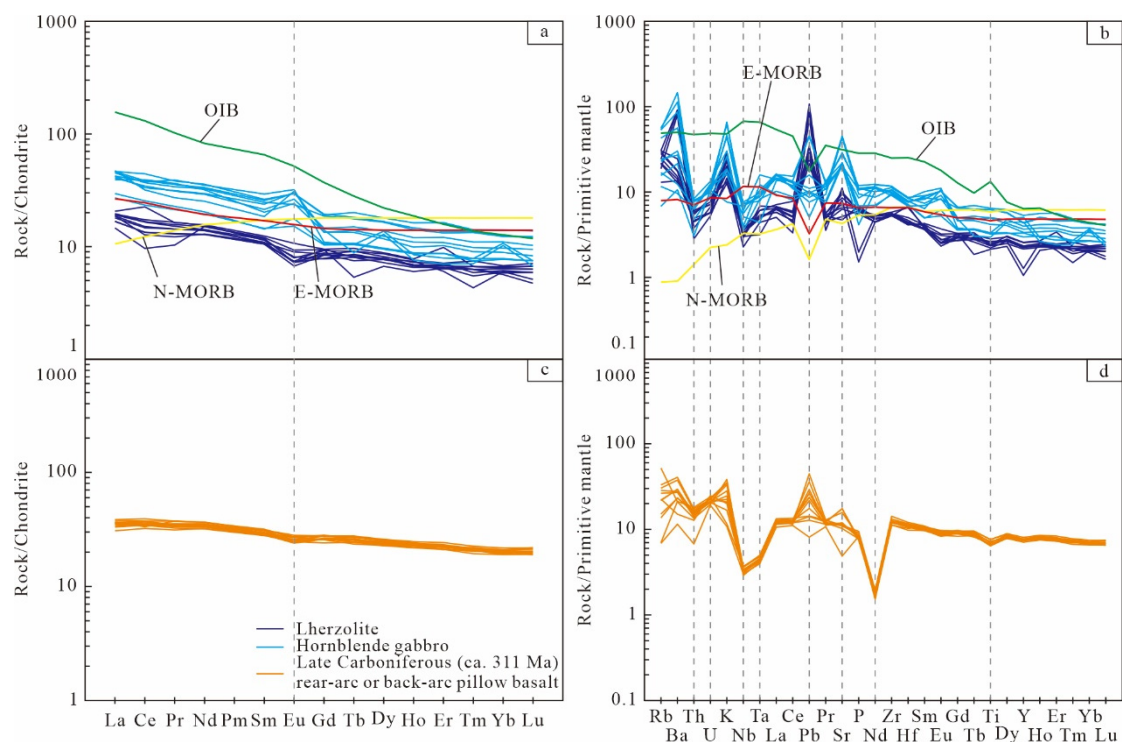


Figure 5. Chondrite-normalized REE patterns (a,c) and primitive mantle normalized multielement diagrams (b,d). Data sources: Late Carboniferous (ca. 311 Ma) rear-arc or back-arc pillow basalt from Xie et al. [35]; normalizing values from Sun and McDonough [39].

4.3. Whole-Rock Sr-Nd Isotopes

Whole-rock Sr-Nd isotopic compositions are listed in Table S3 and shown in Figure 6. For all the mafic–ultramafic rocks in this study, their initial $^{87}\text{Sr}/^{86}\text{Sr}$ ratios and $\epsilon_{\text{Nd}}(t)$ values were calculated based on their magma crystallization age at $t = 306$ Ma.

All the analyzed samples are characterized by depleted isotope compositions, which reflect a depleted mantle source (Figure 6). The Mozbaysay hornblende gabbros and lherzolites have relatively uniform Sr-Nd isotopic compositions, with initial $^{87}\text{Sr}/^{86}\text{Sr}$ and $^{143}\text{Nd}/^{144}\text{Nd}$ values ranging from 0.702989281 to 0.703900955 and 0.512561 to 0.512706, respectively, and their $\epsilon_{\text{Nd}}(t)$ values range from +6.8 to +8.0 and +6.2 to +9.0, respectively (Table S3; Figure 6).

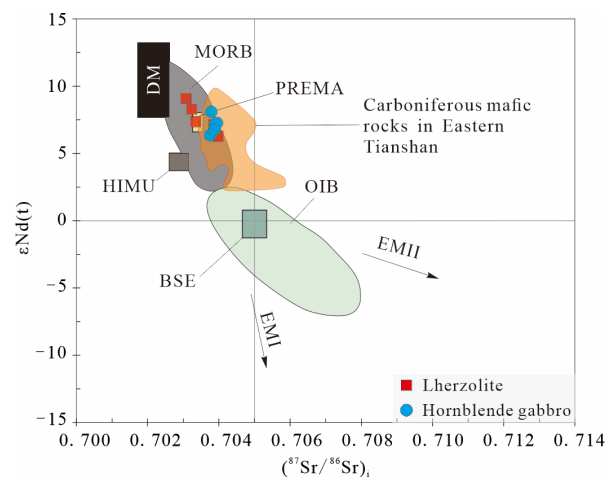


Figure 6. $(^{87}\text{Sr}/^{86}\text{Sr})_i$ versus $\epsilon\text{Nd}(t)$ diagram for the Mozbaysay lherzolites and hornblende gabbros in Balikun area (after [40]). Sr–Nd isotopic data for Carboniferous mafic rocks in eastern North Tianshan is from Zhang et al. [41] and references therein.

5. Discussion

5.1. Assessment of Alteration Effects, Crustal Contamination, and Fractional Crystallization

5.1.1. Alteration Effects and Crustal Contamination

The Mozbaysay mafic–ultramafic rocks have variable high LOI values (2.79–6.45 wt.%) and ubiquitous presence of secondary minerals (i.e., chlorite, epidote, iddingsite, and serpentine) replacing the primary igneous minerals, indicating that they underwent alteration, and the abundance of major oxides, and some mobile trace elements could have been modified. Zr is considered one of the least mobile elements during low-grade alteration and metamorphism, making it a preferred alteration-independent index for assessing the mobility of other trace elements [42–44]. For the Mozbaysay hornblende gabbros, the alkaline earth metals (i.e., Ca and Sr) and alkali metals (i.e., Rb and K) show relatively large content variations and no visible correlation with Zr abundances, indicating they suffered variable degrees of mobility during post-magmatic alteration (Figure 7; [42–45]). On the contrary, the REE, Y, U, and Hf are well correlated with Zr, suggesting that these elements should be immobile during the post-magmatic process. In addition, the transition metal elements (i.e., Cr, Co, and Ni) show consistent trends with Zr, indicating they are relatively immobile (Figure 7; [45]). The alkaline and alkali earth metals, REEs, and transition metal elements of the Mozbaysay lherzolites do not show a correlation with their Zr contents, and variations in concentrations of these elements are small (Figure 7; Table S2), indicating a weak post-magmatic alteration.

In the chondrite-normalized REE and primitive mantle-normalized trace element diagrams, Mozbaysay lherzolites and hornblende gabbros exhibit relatively consistent and smooth patterns with slightly positive to negative Ce and Eu anomalies, which also support the limited mobility of REEs (Figure 5a,b). U and Th of Mozbaysay lherzolites and hornblende gabbros show a clear linear relationship, whereas Pb and Th do not show a clear relationship, indicating some degree of secondary mobility of Pb (Figure 7i–k). Therefore, Mozbaysay lherzolites and hornblende gabbros probably have suffered a post-magmatic alteration to a certain extent, and the following discussion hence mainly focuses on the abundances and ratios of immobile elements.

Generally, crustal contamination is the main mechanism to incorporate the crustal component into mantle-derived magmas during their ascent enroute through the continental crust in accretionary orogens. The crust is depleted in high-frequency elements (e.g., Nb and Ta), and magmas experiencing severe crustal contamination would result in Nb and Ta depletion rather than enrichment [40,46]. However, the Mozbaysay lherzolites and hornblende gabbros are slightly depleted in Nb but rich in Ta (Figure 5b). In addition, the Nb and La contents of the bulk crust (12.00 ppm and 30.00 ppm, respectively [47]) far

outweigh those of the mantle (0.71 ppm and 0.69 ppm, respectively [39]). Hence, even a small amount of crustal contamination can significantly reduce the Nb/La ratio of mantle-derived magmas and induce a positive correlation between MgO and Nb/La ratios [40]. However, the MgO contents and Nb/La ratios of the Mozbaysay mafic–ultramafic rocks lack linear correlations (Figure 8a). Furthermore, the lack of correlation between Th/Nb and La/Sm (Figure 8b) is consistent with no or insignificant crustal contamination as well [48]. Hence, these lines of evidence mentioned above suggest insignificant crustal contamination during the formation of the Mozbaysay lherzolites and hornblende gabbros, and it should be noted that minor crustal contamination cannot be excluded, as suggested by the existence of xenolithic zircons. However, minor assimilation of sedimentary rocks could contribute a disproportionately large number of zircons, but the effect on the bulk-rock element compositions may be negligible [49].

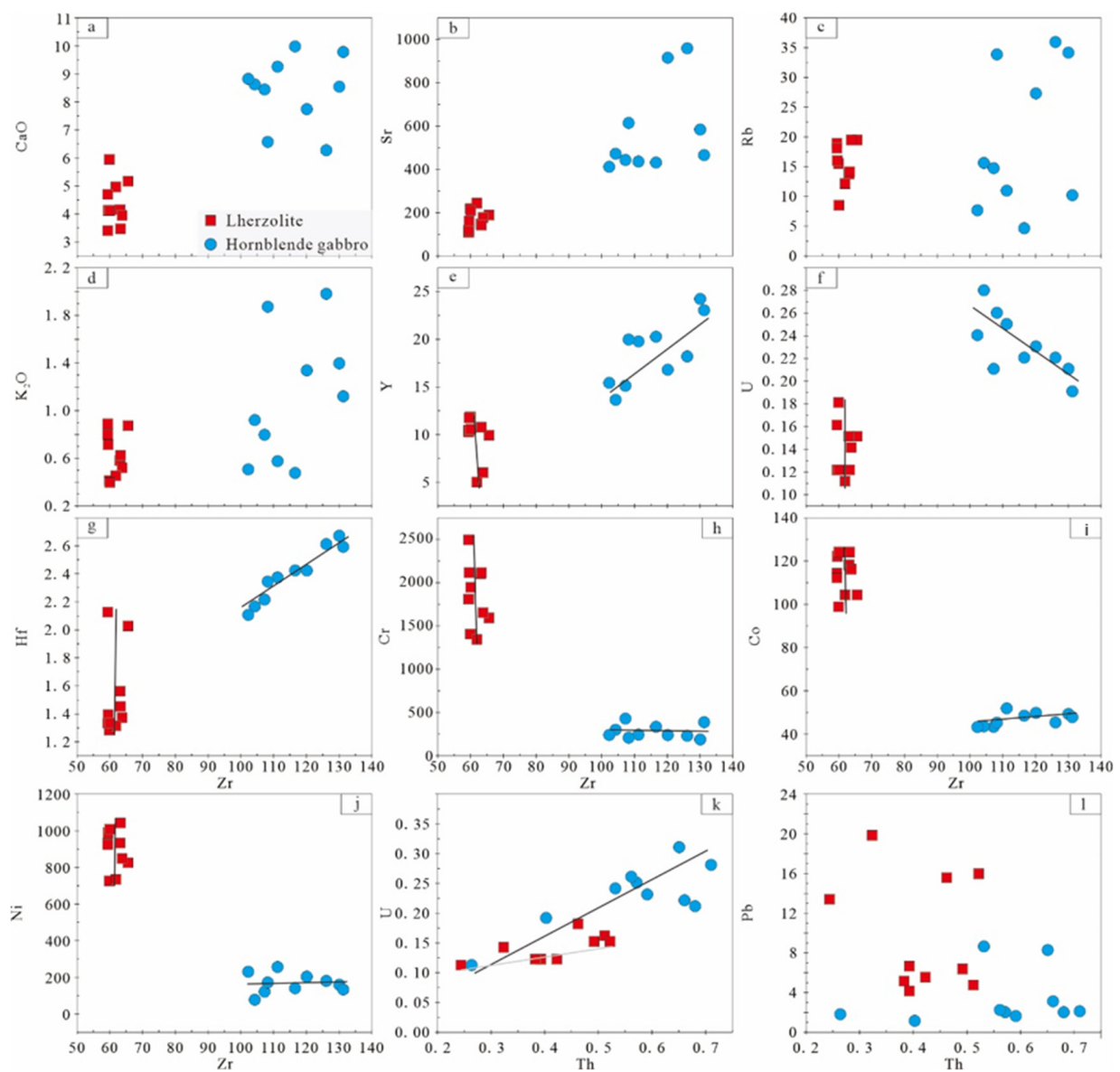


Figure 7. Bivariate plots of elements versus Zr for the Mozbaysay lherzolites and hornblende gabbros to assess the alteration effects (a–l).

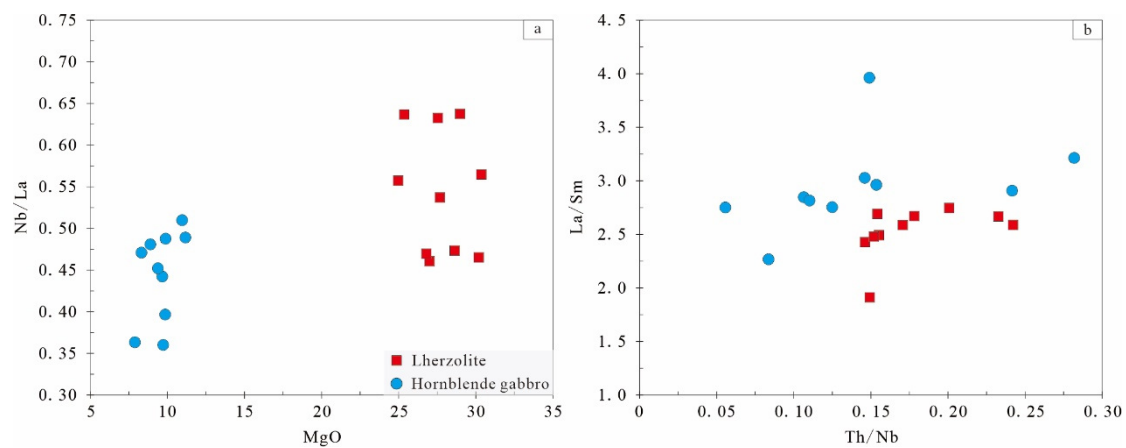


Figure 8. (a) MgO versus Nb/La and (b) Th/Nb versus La/Sm diagram for the Mozbaysay lherzolites and hornblende gabbros to assess the crustal contamination.

5.1.2. Fractional Crystallization

The Mozbaysay mafic–ultramafic rocks have relatively low ($^{87}\text{Sr}/^{86}\text{Sr}$), and high positive ε_{Nd} (t) values (Figure 6), $\text{Mg}^\#$ values (59.82–76.92) together with their Cr (165–2493 ppm), Ni (66.6–1041 ppm) contents, indicating that these complexes have a mantle source. The initial melts were generated from the mantle with Cr > 1000 ppm, Ni > 400 ppm, and $\text{Mg}^\#$ ranging from 73 to 81 [44]. During the melt ascent to the surface, the fractionation of olivine and spinel during the magma evolution may cause decreases in Cr and Ni contents, and $\text{Mg}^\#$ values [39]. The lherzolites have narrow range of $\text{Mg}^\#$ values (74.66–76.92) but variable Ni (722–1041 ppm) and Cr (1332–2493 ppm) contents, which may indicate significant fractionation of olivine and spinel during magma evolution of the lherzolite (Figure 9). Although the hornblende gabbros have variable $\text{Mg}^\#$ values (59.82–72.54), their content ranges of Ni (66.6–247 ppm) and Cr (10.1–24.2 ppm) are relatively lower and narrower compared to those of lherzolites, indicating insignificant fractionation of olivine and spinel during magma evolution (Figure 9). The lherzolites and hornblende gabbros show constant Fe_2O_3 , CaO, and TiO_2 contents (Figure 9c–e), indicating that the Fe–Ti oxide was not a major crystallization phase. The negative correlations of SiO_2 , CaO, Al_2O_3 , and Eu/Eu^* ratios with $\text{Mg}^\#$ and negative Eu anomalies ($\text{Eu}/\text{Eu}^* = 0.71\text{--}0.98$) of lherzolites reflect significant plagioclase fractionation (Figure 9d–h). Amphibole is another possible crystallization phase, but the weak correlation of $\text{Mg}^\#$ and Dy/Yb for lherzolites is inconsistent with the fractionation of amphibole (Figure 9i). For the hornblende gabbros, the correlations of $\text{Mg}^\#$ with SiO_2 , Fe_2O_3 , TiO_2 , and CaO reflect fractionation of clinopyroxene. Their Al_2O_3 contents and Eu/Eu^* ratios show slightly positive correlations with $\text{Mg}^\#$ (Figure 9g,h), which, together with significant positive Eu anomalies ($\text{Eu}/\text{Eu}^* = 1.09\text{--}1.95$), implies limited removal of plagioclase. In addition, the Dy/Yb ratios of hornblende gabbros show a slightly negative correlation with $\text{Mg}^\#$ (Figure 9i), inconsistent with the fractionation of amphibole as well.

Experimental and crystallization modeling results illustrate that the pressure, temperature, and water fugacity of parental magmas control the crystallization sequences and derivative mineral assemblages [50,51]. The high pressure and high H_2O of parental magmas leads to the crystallization of hydrous minerals first (i.e., amphibole and mica) but suppresses plagioclase [51]. The presence of abundant hornblende and some phlogopite in the hornblende gabbros thus implies high water content in their parental magmas (>3 wt.%; Figure 3e,f; [52]). This is the case for the hornblende gabbros that have high contents of Al_2O_3 (15.80–18.87 wt.%) and absence of Eu anomalies (Figure 5a; Table S2). Petrographic observation also reveals a hornblende–plagioclase sequence of fractional crystallization for the hornblende gabbros (Figure 3e,f). However, the absence of abundant hydrous minerals (i.e., hornblende and phlogopite) (Figure 3g,h), low content of Al_2O_3 (6.23–10.58; Table S2), and negative Eu anomalies (Figure 5a) of the lherzolites suggest fractional crystallization

of plagioclase during magma evolution, which is also confirmed by petrographic observation (Figure 3g). Therefore, the primary magmas for the Mozbaysay hornblende gabbros and lherzolites would have different water contents, which in turn indicate that water is enriched in the residual melt during differentiation.

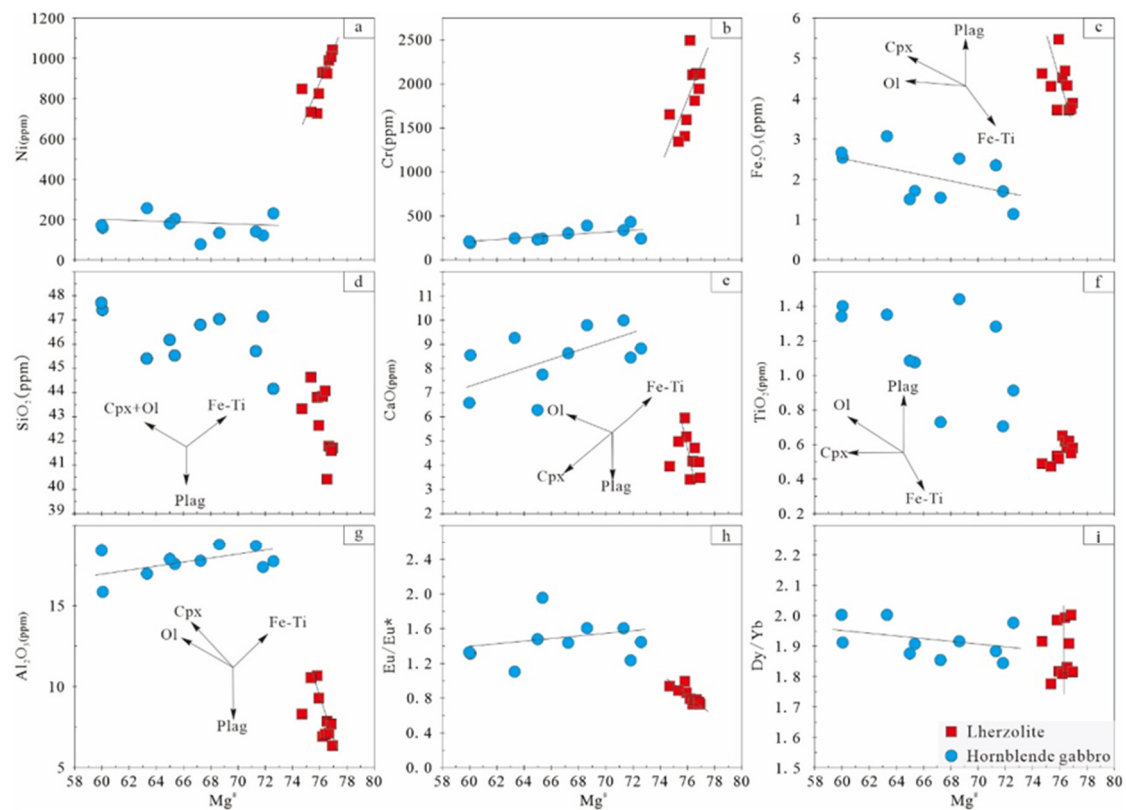


Figure 9. Variations of selected major and trace element contents and ratios versus $Mg^{\#}$ for the Mozbaysay lherzolites and hornblende gabbros (a–i).

5.2. Mantle Metasomatism Induced by Slab–Mantle Interaction

Mantle metasomatism is one of the important pathways leading to the mineralogical and chemical transformation of the mantle [53,54]. Some trace element pairs with close distribution coefficients and resistance to fractionation during the igneous process can be used as tracers for parental magma of igneous rocks [55]. For example, Nb/La (ca. 1.18), Ta/U (ca. 2.7), Nb/U (ca. 47), and Ce/Pb (=25) ratios are relatively consistent in MORB and OIB [39]. The large deviation of these values would indicate the non-magma evolution processes have fractionated these elements from their magma sources, such as a subduction-related process before the partial melting of the mantle sources [55]. The Mozbaysay mafic–ultramafic rocks have varied ratios of Nb/La (0.36–0.87), Ta/U (2.11–5.47), Nb/U (17.04–22.42), and Ce/Pb (0.39–13.98) (Table S2). In the Th/Yb–Nb/Yb diagram, these mafic–ultramafic rocks are plotted above the MORB–OIB mantle array (Figure 10a), indicating the involvement of subduction-modified components within the mantle source.

Trace element compositions of magmas generated from slab–mantle interaction metasomatized mantle mainly include contributions from two components, i.e., hydrous fluids from the subducted slab and melts from subducted sediments [56,57]. The aqueous fluids from dehydration of the subducted slab are relatively enriched in fluid mobile elements (e.g., Rb, Ba, U, and Th [56,58]), while melts from subducted sediments generally enrich LILEs and LREEs with small fractionations [55]. The Mozbaysay mafic–ultramafic rocks show large fractionation of fluid mobile elements with relatively high Ba/Nb ratios (Table S2) and consistently follow a trend of fluid-related enrichment, revealing a significant contribution from hydrous fluids rather than sediment melts (Figure 10b).

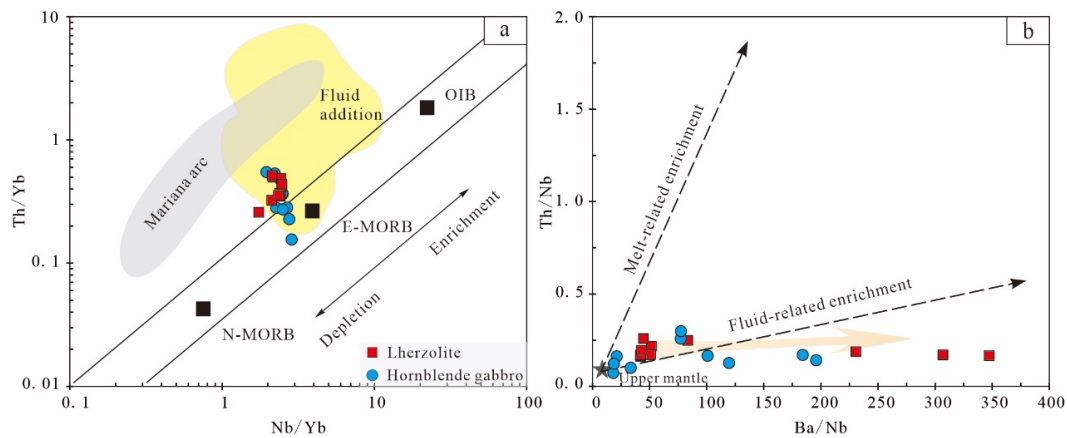


Figure 10. Elements ratios discriminating between slab-derived fluid components versus melt components. (a) Th/Yb versus Nb/Yb diagram (after [59]), data of slab fluid-enriched basaltic rocks are from [60]; (b) Ba/Nb versus Th/Nb diagram (after [57]), upper mantle (UM)-derived melts are from Gale et al. [9].

5.3. Heterogeneous Mantle Sources for Mozbaysay Lherzolites and Hornblende Gabbros

As discussed in the preceding section, post-magmatic alteration and crustal contamination can be excluded as possible causes for distinctive geochemical characteristics between Mozbaysay lherzolites and hornblende gabbros. Their specific compositional features, therefore, were probably inherited from their mantle sources. They have La/Yb (2.98–6.79) and Ti/V (22.63–39.10) ratios close to MORB (La/Yb = 1.39 [39,61]) but distinct from OIB (La/Yb = 0.82; Figure 11a; [39,61]). In addition, the OIB source component generally has diagnostic high Nb and Ta contents [39,62] in contrast to the Mozbaysay lherzolites and hornblende gabbros that have Nb depletions and slight Ta enrichment (Figure 5b). Additionally, the $\epsilon_{Nd}(t)$ values of the Mozbaysay lherzolites and hornblende gabbros are broadly higher than even those of the most depleted end member of the mantle plume (Figure 6). Furthermore, these mafic–ultramafic rocks exhibit slightly LREE-enriched and flat HREE patterns with minor (slightly positive to negative) Eu anomalies, comparable to typical E-MORB (Figure 5a). Therefore, the above lines of evidence suggest that the mantle source of the Mozbaysay lherzolites and hornblende gabbros shows affinities of E-MORB rather than OIB; hence, they should not be related to a mantle plume. The narrow range and radiogenic Nd isotopic compositions of the Mozbaysay lherzolites ($\epsilon_{Nd}(t) = +6.2$ to $+9.0$) and hornblende gabbros ($\epsilon_{Nd}(t) = +6.3$ to $+8.0$) suggest their mantle magma source is relatively homogeneous and depleted, which is most likely a mixture of melts of the asthenospheric and lithospheric mantle sources (Figure 11b).

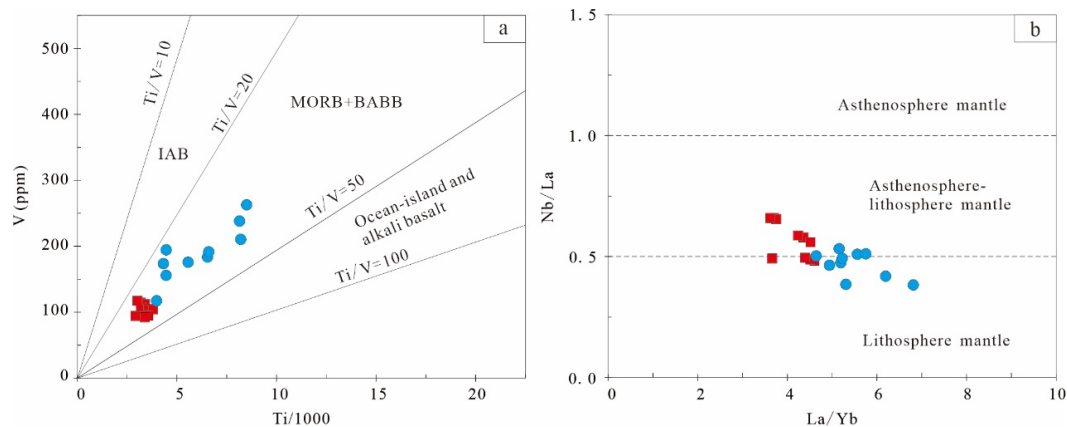


Figure 11. (a) Ti versus V diagram (after [61]); (b) La/Yb versus Nb/La diagram (after [63]).

5.4. Slab Breakoff Triggered Shallow Depth Lithosphere–Asthenosphere Interaction for Generating the Mozbaysay Mafic–Ultramafic Rocks

The REE fraction patterns of igneous rocks can reveal the partial melting degree of a magma source and the thickness of the lithosphere [64–66]. The Mozbaysay hornblende gabbros and lherzolites have minor fractionation with the $(La/Yb)_N$ values from 2.56 to 3.27 and from 3.30 to 4.87, respectively. These values are distinct from the partition coefficients of garnet ($Kd_{Yb}^{Grt/L} / Kd_{La}^{Grt/L} \approx 7000$) but comparable to that of spinel ($Kd_{Yb}^{Sp/L} / Kd_{La}^{Sp/L} \approx 1$) [67], suggesting a shallow spinel peridotite mantle source ([68]; Figure 12a). In addition, there is consensus that garnet has a high partition coefficient for Yb relative to Gd and Dy, and partial melting of a garnet peridotite mantle therefore causes strong fractionation of Dy/Yb and Gd/Yb [69]. On the contrary, spinel has similar partition coefficients for Yb, Gd, and Dy, and Dy/Yb and Gd/Yb are slightly fractionated during melting in the spinel stability field [66]. The Mozbaysay hornblende gabbros and lherzolites possess low Dy/Yb and Gd/Yb ratios, which plot along the melting curve of spinel peridotite (Figure 12b), indicating that partial melting took place at a relatively shallow depth, dominantly within the spinel stability field. As the transition from garnet to spinel occurs in the mantle at a depth of ca. 70–80 km [70], the decompression melting probably took place at a shallower depth (<ca. 80 km). Therefore, it seems quite likely that the lithosphere was locally thinned to allow for decompression melting of the asthenosphere.

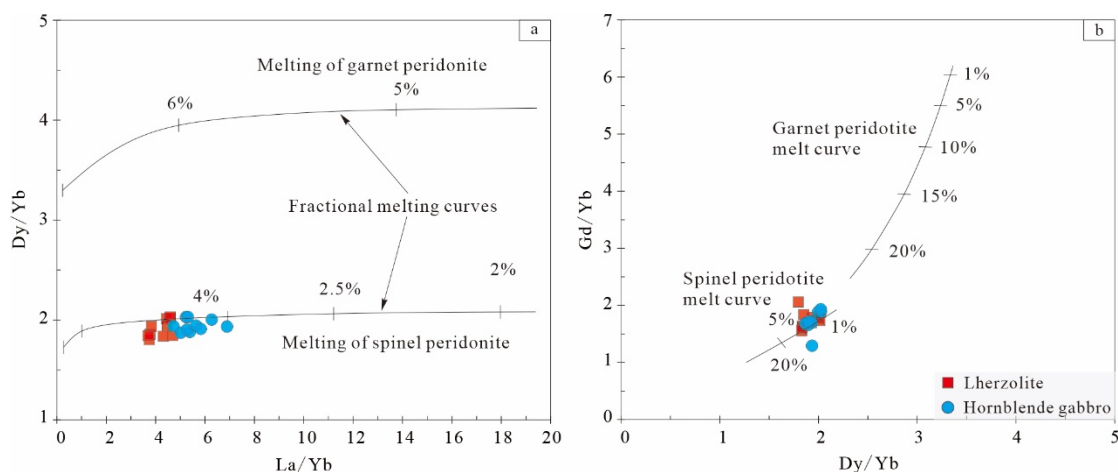


Figure 12. (a) La/Yb versus Dy/Yb diagram (after [71]); (b) Gd/Yb versus Dy/Yb diagram (after [72]).

Therefore, we suggest that the Mozbaysay hornblende gabbros and lherzolites were likely derived from a depleted spinel–facies mantle source at shallow depths of <ca. 80 km induced by an upwelling asthenosphere in an extensional geodynamic setting.

Three mechanisms have been proposed to explain the asthenospheric thinning during orogenesis, including convective thinning of the lithospheric root [73], gravity-induced delamination of orogenic root [74], and slab breakoff [75]. The former two mechanisms would generate widespread and intensive asthenosphere-derived mafic magmas and granitoids, respectively [73,74]. However, the Late Carboniferous magmatism in the NTB is sporadically distributed linearly along terrane boundaries in small volume (Figure 1b). Therefore, we suggest that decompression-induced influx of asthenospheric heat and melts through slab window, as well as the partial melting of the lithospheric mantle at a shallow depth in an extensional geodynamic setting during slab breakoff, should be the most likely mechanism producing the Mozbaysay hornblende gabbros and lherzolites.

5.5. Implications for the Tectonic Transitional Mechanism from Subduction to Post-Collision in NTB

Late Carboniferous to Early Permian is a crucial tectonic period for the NTB during which various tectonic blocks were finally consolidated following the closure of branches

of the Paleo-Asian Ocean (i.e., the North Tianshan Ocean in the south and Kalamaili ocean in the north), thus constituting the tectonic transition from subduction to post-collisional extension (Figure 1b; [4–7]). Unfortunately, the geological records, i.e., synorogenic deformation, sedimentation, and even magmatism during this tectonic transition, were generally destroyed or obscured by later geological events, making it hard to reveal such tectonic transitions, and the nature and timing of this tectonic transition remain controversial [4,7].

The Late Carboniferous arc-related pillow basalts indicate that the subduction of the oceanic lithosphere beneath the NTB lasted at least until ca. 311 Ma and exhibit significant negative Nb, Ta, Nd, and Ti anomalies compared with Mozbaysay hornblende gabbros and Iherzolites (Figure 5c,d; [35]). While the Early Permian (ca. 297–285 Ma) magmatism in this belt is characterized by A-type and I-type granites, mafic dykes, mafic–ultramafic complexes, and bimodal volcanic rocks, the generation of this phase magmatism requires a lithosphere extension and the upwelling of the asthenosphere. It is widely accepted that this magmatism was formed in a post-collision tectonic setting [16,17,24,25,28,41,76–79]. This hypothesis is further supported by the Permian post-collisional features, e.g., continental molasse formation, ancient flora, paleomagnetism, regional unconformity, regional transcurrent tectonics [80], and graben or pull apart-related underwater rockslide avalanche accumulation [81]. Therefore, the tectonic transition from subduction to post-collision in NTB likely occurred during the ca. 311–297 Ma period (Figure 13a).

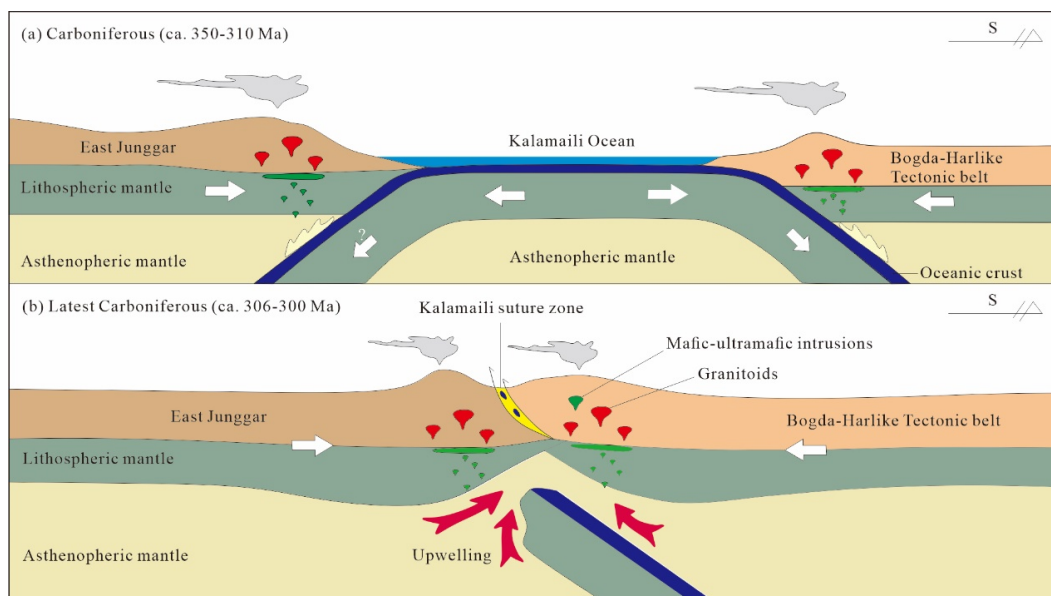


Figure 13. Schematic cartoons illustrating tectonic evolution of the Bogda–Harlike tectonic belt, Eastern Tianshan during the Carboniferous period. (a) Carboniferous (ca. 350–310 Ma) bidirectional and/or unidirectional subduction of the Kalamaili Ocean; (b) Late Carboniferous (306–300 Ma) breakoff of oceanic lithosphere soon after the closure of the Kalamaili Ocean, leading to partial melting of upwelling asthenospheric mantle and overlying lithospheric mantle.

Slab breakoff usually occurs at the initial stages of continental collision, due to the contrasting strength and buoyancy between the subducting oceanic lithosphere and the dragging continental lithosphere. Slab breakoff is triggered by the attempted subduction of the continental lithosphere following the continental collision and the opposing buoyancy forces between the dense oceanic lithosphere and the buoyant continental lithosphere [75]. With the lateral propagation of slab detachment, the hot asthenospheric mantle rises through the linear lithospheric gap and causes a thermal anomaly in the mantle wedge and partial melting of the overriding lithospheric mantle [82]. Hence, the identification of magmatism related to slab breakoff is an effective tool for determining the tectonic transition from subduction to post-collision in an ancient orogenic belt [41,83,84].

The petrogenetic links of the Mozbaysay hornblende gabbros and lherzolites (ca. 306 Ma; this study), Hongshankou Nb-enriched dolerites (305–302 Ma [41]), and Shiquanzi post-collisional gabbro (ca. 301 ± 6 Ma [16]) in the NTB with slab breakoff suggest that the tectonic transition in the NTB most likely initiated in situ at ca. 306 Ma and lasted until ca. 300 Ma (Figure 13b).

6. Conclusions

The Mozbaysay mafic–ultramafic complex in the Qijiaojing–Balikun area, eastern North Tianshan, was emplaced in the Late Carboniferous period at ca. 306 Ma. Analysis of petrological, elemental, and isotopic data indicates that the Mozbaysay hornblende gabbro and lherzolite were crystallized from a mixture of melts of lithospheric and asthenospheric mantle sources, which were metasomatized by aqueous fluids coming from the dehydration of the subducted slab during slab–mantle interaction. The interaction between the asthenospheric heat and melts with the overlying lithospheric mantle corresponds to a lithosphere extension and stress relaxation scenario. Therefore, the slab break-off seems to be the most plausible mechanism to explain the geochemical characteristics. The petrogenetic links of the Late Carboniferous mafic–ultramafic rocks in eastern North Tianshan with slab breakoff suggest that the tectonic transition most likely initiated in situ at ca. 306–305 Ma and lasted until ca. 300 Ma.

Supplementary Materials: The following supporting information can be downloaded at: <https://www.mdpi.com/article/10.3390/min13101293/s1>, Table S1: Zircon U–Pb ages of the Mozbaysay hornblende gabbro; Table S2: Whole-rock major and trace elements of the Mozbaysay lherzolites and hornblende gabbros in this study; Table S3: Sr–Nd isotopic compositions of the Mozbaysay lherzolites and hornblende gabbros in this study. References [85–87] are cited in the supplementary materials.

Author Contributions: Conceptualization, F.G. and Y.C.; methodology, X.L.; software, Z.L.; validation, F.G., Y.C. and R.G.; formal analysis, X.L.; investigation, X.L.; resources, Y.C.; data curation, Z.L.; writing—original draft preparation, F.G.; writing—review and editing, F.G.; visualization, Z.L.; supervision, Y.C.; project administration, R.G.; funding acquisition, F.G. All authors have read and agreed to the published version of the manuscript.

Funding: This research was funded by Natural Science Foundation of Xinjiang Province, grant number 2022D01C80; Tianchi Doctoral Project of Xinjiang Province, grant number TCBS202107; Doctoral Research Startup Funds of Xinjiang University, grant number 620321013 and Basic Scientific Research Funds and Research Projects of Universities in the Autonomous Region, grant number 610223038.

Acknowledgments: We appreciate the constructive suggestions from the editor-in-chief and three anonymous reviewers, which helped us to evaluate our manuscript. This research was supported by the Natural Science Foundation of Xinjiang Province (2022D01C80), the Tianchi Doctoral Project of Xinjiang Province (TCBS202107), the Doctoral Research Startup Funds of Xinjiang University (620321013), and the Basic Scientific Research Funds and Research Projects of Universities in the Autonomous Region (610223038).

Conflicts of Interest: The authors declare no conflict of interest.

References

- Şengör, A.M.C.; Natal'in, B.A.; Burtman, V.S. Evolution of the Altaid tectonic collage and Paleozoic crustal growth in Eurasia. *Nature* **1993**, *364*, 299–307. [[CrossRef](#)]
- Windley, B.F.; Alexeev, D.; Xiao, W.J.; Kröner, A.; Badarch, G. Tectonic Models for Accretion of the Central Asian Orogenic Belt. *J. Geol. Soc.* **2007**, *164*, 31–47. [[CrossRef](#)]
- Safonova, I. Juvenile versus recycled crust in the Central Asian Orogenic Belt: Implications from ocean plate stratigraphy, blueschist belts and intra-oceanic arcs. *Gondwana Res.* **2017**, *47*, 6–27. [[CrossRef](#)]
- Xiao, W.J.; Windley, B.F.; Han, C.M.; Liu, W.; Wan, B.; Zhang, J.E.; Ao, S.J.; Zhang, Z.Y.; Song, D.F. Late Paleozoic to early Triassic multiple roll-back and oroclinal bending of the Mongolia collage in Central Asia. *Earth-Sci. Rev.* **2018**, *186*, 94–128. [[CrossRef](#)]
- Wartes, M.A.; Carroll, A.R.; Greene, T.J. Permian sedimentary record of the Turpan-Hami basin and adjacent regions, northwest China: Constraints on post amalgamation tectonic evolution. *Geol. Soc. Am. Bull.* **2002**, *114*, 131–152. [[CrossRef](#)]

6. Charvet, J.; Shu, L.S.; Laurent-Charvet, S. Paleozoic structural and geodynamic evolution of eastern Tianshan (NW China): Welding of the Tarim and Junggar plates. *Epis. J. Int. Geosci.* **2007**, *30*, 162–186.
7. Han, Y.G.; Zhao, G.C. Final amalgamation of the Tianshan and Junggar orogenic collage in the southwestern Central Asian Orogenic Belt: Constraints on the closure of the Paleo-Asian Ocean. *Earth-Sci. Rev.* **2018**, *186*, 129–152. [[CrossRef](#)]
8. Bonin, B. Do coeval mafic and felsic magmas in post-collisional to within-plate regimes necessarily imply two contrasting, mantle and crustal, sources? A review. *Lithos* **2004**, *78*, 1–24. [[CrossRef](#)]
9. Gale, A.; Dalton, C.A.; Langmuir, C.H.; Su, Y.J.; Schilling, J.G. The mean composition of ocean ridge basalts. *Geochem. Geophys. Geosyst.* **2013**, *14*, 489–518. [[CrossRef](#)]
10. Pirajno, F.; Mao, J.W.; Zhang, Z.C.; Zhang, Z.H.; Chai, F.M. The association of mafic-ultramafic intrusions and A-type magmatism in the Tian Shan and Altay orogens, NW China: Implications for geodynamic evolution and potential for the discovery of new ore deposits. *J. Asian Earth Sci.* **2008**, *32*, 165–183. [[CrossRef](#)]
11. Ao, S.J.; Xiao, W.J.; Han, C.M.; Mao, Q.G.; Zhang, J.E. Geochronology and geochemistry of Early Permian mafic-ultramafic complexes in the Beishan area, Xinjiang, NW China: Implications for late Paleozoic tectonic evolution of the southern Altai. *Gondwana Res.* **2010**, *18*, 466–478. [[CrossRef](#)]
12. Su, B.X.; Qin, K.Z.; Zhou, M.F.; Sakyi, P.A.; Thakurta, J.; Tang, D.M.; Liu, P.P.; Xiao, Q.H.; Sun, H. Petrological, geochemical and geochronological constraints on the origin of the Xiadong Ural-Alaskan type complex in NW China and tectonic implication for the evolution of southern Central Asian Orogenic Belt. *Lithos* **2014**, *200–201*, 226–240. [[CrossRef](#)]
13. Mao, Q.G.; Ao, S.J.; Windley, B.F.; Zhang, Z.Y.; Song, D.F.; Zhang, J.E.; Wan, B.; Tan, W.; Han, C.M.; Xiao, W.J. Petrogenesis of Late Carboniferous-Early Permian mafic-ultramafic-felsic complexes in the eastern Central Tianshan, NW China: The result of subduction-related transtension? *Gondwana Res.* **2021**, *95*, 72–87. [[CrossRef](#)]
14. Cui, X.; Sun, M.; Zhao, G.C.; Zhang, Y.Y. Origin of Permian mafic intrusions in southern Chinese Altai, Central Asian Orogenic Belt: A post-collisional extension system triggered by slab break-off. *Lithos* **2021**, *390–391*, 106112. [[CrossRef](#)]
15. Lu, Y.Y.; Lesher, C.M.; Deng, J. Geochemistry and genesis of magmatic Ni-Cu-(PGE) and PGE-(Cu)-(Ni) deposits in China. *Ore Geol. Rev.* **2019**, *107*, 863–887. [[CrossRef](#)]
16. Yuan, C.; Sun, M.; Wilde, S.; Xiao, W.J.; Xu, Y.G.; Long, X.P.; Zhao, G.C. Post-collisional plutons in the Balikun area, East Chinese Tianshan: Evolving magmatism in response to extension and slab break-off. *Lithos* **2010**, *119*, 269–288. [[CrossRef](#)]
17. Chen, B.Y.; Yu, J.J.; Liu, S.J. Source characteristics and tectonic setting of mafic-ultramafic intrusions in North Xinjiang, NW China: Insights from the petrology and geochemistry of the Lubei mafic-ultramafic intrusion. *Lithos* **2018**, *308–309*, 329–345. [[CrossRef](#)]
18. Guo, Z.J.; Han, B.F.; Zhang, Y.Y.; Chen, S. Mesozoic and Cenozoic crust-mantle interaction in the Central Asian Orogenic Belt: A comparative study of mantle-derived magmatic rocks in northern Xinjiang. *Acta Petrol. Sin.* **2010**, *26*, 431–439, (In Chinese with English Abstract).
19. Sun, M.; Wang, Y.H.; Zhang, F.F.; Lin, S.Y.; Xue, C.J.; Liu, J.J.; Zhu, D.C.; Wang, K.; Zhang, W. Petrogenesis of Late Carboniferous intrusions in the Linglong area of Eastern Tianshan, NW China, and tectonic implications: Geochronological, geochemical, and zircon Hf-O isotopic constraints. *Ore Geol. Rev.* **2020**, *120*, 103462. [[CrossRef](#)]
20. Tang, D.M.; Qin, K.Z.; Su, B.X.; Mao, Y.J.; Evans, N.J.; Fang, L.R. Addition of H₂O at the Baishiquan and Tianyu magmatic Ni-Cu sulfide deposits, southern Central Asian Orogenic Belt, China: Evidence from isotopic geochemistry of olivine and zircon. *Miner. Depos.* **2021**, *57*, 235–254. [[CrossRef](#)]
21. Xiao, W.J.; Zhang, L.C.; Qin, K.Z.; Sun, S.; Li, J.L. Paleozoic accretionary and collisional tectonics of the eastern Tianshan (China): Implications for the continental growth of central Asia. *Am. J. Sci.* **2004**, *304*, 370–395. [[CrossRef](#)]
22. Xiao, W.J.; Windley, B.F.; Yuan, C.; Sun, M.; Han, C.M.; Lin, S.F.; Chen, H.L.; Yan, Q.R.; Liu, D.Y.; Qin, K.Z.; et al. Paleozoic multiple subduction-accretion processes of the southern Altai. *Am. J. Sci.* **2009**, *309*, 221–270. [[CrossRef](#)]
23. Xiao, W.J.; Kröner, A.; Windley, B. Geodynamic evolution of Central Asia in the Paleozoic and Mesozoic. *Int. J. Earth Sci.* **2009**, *98*, 1185–1188. [[CrossRef](#)]
24. Chen, X.J.; Zhang, K.H.; Zhang, G.L.; Zhou, J. Geochronology and geochemistry characteristics of the Early Permian monzogranite and dioritic enclaves of East Tianshan and their tectonic implications. *Acta Geol. Sin.* **2016**, *90*, 2334–2354, (In Chinese with English Abstract).
25. Chen, X.J.; Zhang, K.H.; Zhang, G.L.; Zhou, J. Characteristics, petrogenesis and tectonic implications of the Permian Omoertage alkaline granites in Harlik area, Xinjiang. *Acta Petrol. Et Mineral.* **2016**, *35*, 929–946, (In Chinese with English Abstract).
26. Gao, J.F.; Zhou, M.F. Generation and evolution of siliceous high magnesium basaltic magmas in the formation of the Permian Huangshandong intrusion (Xinjiang, NW China). *Lithos* **2013**, *162*, 128–139. [[CrossRef](#)]
27. Deng, Y.F.; Song, X.Y.; Hollings, P.; Zhou, T.; Yuan, F.; Chen, L.M.; Zhang, D. Role of asthenosphere and lithosphere in the genesis of the Early Permian Huangshan mafic-ultramafic intrusion in the Northern Tianshan, NW China. *Lithos* **2015**, *227*, 241–254. [[CrossRef](#)]
28. Song, P.; Wang, T.; Tong, Y.; Zhang, J.; Huang, H. Late Carboniferous intrusions along the Kalamaili suture zone, southwestern Central Asian Orogenic Belt (CAOB): Implications for a tectonic switch from subduction to collision. *Int. Geol. Rev.* **2023**, *65*, 1601–1621. [[CrossRef](#)]
29. Qin, K.Z.; Su, B.X.; Sakyi, P.A.; Tang, D.M.; Li, X.H.; Sun, H.; Xiao, Q.H.; Liu, P.P. SIMS zircon U-Pb geochronology and Sr-Nd isotopes of Ni-Cu-Bearing Mafic-Ultramafic Intrusions in Eastern Tianshan and Beishan in correlation with flood basalts in Tarim Basin (NW China): Constraints on a ca. 280 Ma mantle plume. *Am. J. Sci.* **2011**, *311*, 237–260. [[CrossRef](#)]
30. Zhang, C.L.; Li, Z.X.; Li, X.H.; Xu, Y.G.; Zhou, G.; Ye, H.M. A Permian large igneous province in Tarim and Central Asian orogenic belt, NW China: Results of a ca. 275 Ma mantle plume? *Geol. Soc. Am. Bull.* **2010**, *122*, 2020–2040. [[CrossRef](#)]

31. Xia, L.Q.; Li, X.M. Revisiting the tectonic setting of the Carboniferous volcanic rocks in the Chinese Tianshan and its neighboring areas. *Gondwana Res.* **2020**, *84*, 1–19. [[CrossRef](#)]
32. Jahn, B.M. The Central Asian Orogenic Belt and growth of the continental crust in the Phanerozoic. *Geol. Soc. Lond. Spec. Publ.* **2004**, *226*, 73–100. [[CrossRef](#)]
33. Li, Y.; Guo, J.F.; Xiao, L.; Lei, W.S.; Li, X.C.; Liu, J.F.; Zheng, Y.J.; Zhou, J. *Xinjiang Uygur Autonomous Region Sandaozhang 1:250000 Regional Geological Survey Report (Revised)*; Geological Survey and Research Institute of Chang'an University: Xi'an, China, 2012; (In Chinese with English Abstract).
34. Xinjiang Bureau of Geology and Mineral Resources. *Regional Geology of Xinjiang Uygur Autonomous Region*; Geological Publishing House: Beijing, China, 1993; (In Chinese with English Abstract).
35. Xie, W.; Luo, Z.Y.; Xu, Y.G.; Chen, Y.B.; Hong, L.B.; Ma, L.; Ma, Q. Petrogenesis and geochemistry of the Late Carboniferous rear-arc (or back-arc) pillow basaltic lava in the Bogda Mountains, Chinese North Tianshan. *Lithos* **2016**, *244*, 30–42. [[CrossRef](#)]
36. Xie, W.; Xu, Y.G.; Chen, Y.B.; Luo, Z.Y.; Hong, L.B.; Ma, L.; Liu, H.Q. High-alumina basalts from the Bogda Mountains suggest an arc setting for Chinese Northern Tianshan during the Late Carboniferous. *Lithos* **2016**, *256–257*, 165–181. [[CrossRef](#)]
37. Zhang, Y.Y.; Sun, M.; Yuan, C.; Long, X.P.; Jiang, Y.D.; Li, P.F.; Huang, Z.Y.; Du, L. Alternating Trench Advance and Retreat: Insights from Paleozoic Magmatism in the Eastern Tianshan, Central Asian Orogenic Belt. *Tectonics* **2018**, *37*, 2142–2164. [[CrossRef](#)]
38. Li, J.Y. Paleozoic active margin slices in the southern Turfan-Hami basin: Geological records of subduction of the Paleo-Asian Ocean plate in central Asian regions. *Acta Petrol. Sin.* **2006**, *22*, 1087–1102, (In Chinese with English Abstract).
39. Sun, S.S.; McDonough, W.F. Chemical and isotopic systematics of oceanic basalts: Implications for mantle composition and processes. *Geol. Soc. Lond. Spec. Publ.* **1989**, *42*, 313–345. [[CrossRef](#)]
40. Huang, Q.T.; Zhang, C.L.; Zhang, K.J.; Hua, Y.J.; Chen, W.C.; Cao, Y.D.; Cheng, P. Interaction of upwelling asthenosphere with oceanic lithospheric mantle in Bangong-Nujiang subduction zone: A new mechanism for the petrogenesis of Nb-enriched basalts. *Lithos* **2023**, *448–449*, 107172. [[CrossRef](#)]
41. Zhang, Y.Y.; Yuan, C.; Sun, M.; Long, X.P.; Huang, Z.Y.; Jiang, Y.D.; Li, P.F.; Du, L. Two late Carboniferous belts of Nb-enriched mafic magmatism in the Eastern Tianshan: Heterogeneous mantle sources and geodynamic implications. *GSA Bull.* **2020**, *132*, 1863–1880. [[CrossRef](#)]
42. Pearce, J.A.; Peate, D.W. Tectonic implications of the composition of volcanic arc magmas. *Annu. Rev. Earth Planet. Sci.* **1995**, *23*, 251–285. [[CrossRef](#)]
43. Winchester, J.A.; Floyd, P.A. Geochemical magma type discrimination: Application to altered and metamorphosed basic igneous rocks. *Earth Planet. Sci. Lett.* **1976**, *28*, 459–469. [[CrossRef](#)]
44. Polat, A.; Hofmann, A.W.; Rosing, M.T. Boninite-like volcanic rocks in the 3.7–3.8 Ga Isua greenstone belt, West Greenland: Geochemical evidence for intra-oceanic subduction zone processes in the early Earth. *Chem. Geol.* **2002**, *184*, 231–254. [[CrossRef](#)]
45. Polat, A.; Hofmann, A.W. Alteration and geochemical patterns in the 3.7–3.8 Ga Isua greenstone belt, West Greenland. *Precambrian Res.* **2003**, *126*, 197–218. [[CrossRef](#)]
46. Liu, H.C.; Wang, Y.J.; Cawood, P.A.; Guo, X.F. Episodic slab rollback and back-arc extension in the Yunnan-Burma region: Insights from Cretaceous Nb-enriched and oceanic-island basalt-like mafic rocks. *Geol. Soc. Am. Bull.* **2017**, *129*, 698–714. [[CrossRef](#)]
47. Taylor, S.R.; McLennan, S.M. *The Continental Crust: Its Composition and Evolution*; Blackwell Scientific Publications: Oxford, UK, 1985.
48. Mackie, R.A.; Scoates, J.S.; Weis, D.; Maerschalk, C.; Peck, D. Trace element and Hf-Nd isotopic profiling of crustal contamination across the marginal zone of the Muskox intrusion, Nunavut. *Geochim. Cosmochim. Acta Suppl.* **2005**, *69*, A863.
49. Wang, Q.; Wyman, D.A.; Xu, J.F.; Wan, Y.S.; Li, C.F.; Jiang, Z.; Qiu, H.; Chu, Z.; Zhao, Z.; et al. Triassic Nb-enriched basalts, magnesian andesites, and adakites of the Qiangtang terrane (Central Tibet): Evidence for metasomatism by slab-derived melts in the mantle wedge. *Contrib. Mineral. Petrol.* **2007**, *155*, 473–490. [[CrossRef](#)]
50. Gaetani, G.A.; Grove, T.L.; Bryan, W.B. The influence of water on the petrogenesis of subduction-related igneous rocks. *Nature* **1993**, *365*, 332–334. [[CrossRef](#)]
51. Müntener, O.; Kelemen, P.B.; Grove, T.L. The role of H₂O during crystallization of primitive arc magmas under uppermost mantle conditions and genesis of igneous pyroxenites: An experimental study. *Contrib. Mineral. Petrol.* **2001**, *141*, 643–658. [[CrossRef](#)]
52. Sisson, T.W.; Grove, T.L. Experimental investigations of the role of H₂O in calc-alkaline differentiation and subduction zone magmatism. *Contrib. Mineral. Petrol.* **1993**, *113*, 143–166. [[CrossRef](#)]
53. Ionov, D.A.; Doucet, L.S.; Ashchepkov, I.V. Composition of the lithospheric mantle in the Siberian craton: New constraints from fresh peridotites in the Udachnaya-East kimberlite. *J. Petrol.* **2010**, *51*, 2177–2210. [[CrossRef](#)]
54. O'Reilly, S.Y.; Griffin, W.L. Mantle metasomatism. In *Metasomatism and the Chemical Transformation of Rock*; Springer: Berlin/Heidelberg, Germany, 2013; pp. 471–533.
55. Kelemen, P.B.; Hanghøj, K.; Greene, A.R. One view of the geochemistry of subduction-related magmatic arcs, with an emphasis on primitive andesite and lower crust. In *Treatise on Geochemistry*; Elsevier: Amsterdam, The Netherlands, 2003; Volume 3, pp. 593–659.
56. Hawkesworth, C.J.; Gallagher, K.; Hergt, J.M.; McDermott, F. Mantle and slab contributions in arc magmas. *Annu. Rev. Earth Planet. Sci.* **1993**, *21*, 175–204. [[CrossRef](#)]
57. Zamboni, D.; Gazel, E.; Ryan, J.G.; Cannatelli, C.; Lucchi, F.; Atlas, Z.D.; Trela, J.; Mazza, S.E.; De Vivo, B. Contrasting sediment melt and fluid signatures for magma components in the Aeolian Arc: Implications for numerical modeling of subduction systems. *Geochem. Geophys. Geosyst.* **2016**, *17*, 2034–2053. [[CrossRef](#)]

58. Shervais, J.W.; Jean, M.M. Inside the subduction factory: Modeling fluid mobile element enrichment in the mantle wedge above a subduction zone. *Geochim. Cosmochim. Acta* **2012**, *95*, 270–285. [[CrossRef](#)]
59. Pearce, J.A. Geochemical fingerprinting of oceanic basalts with applications to ophiolite classification and the search for Archean oceanic crust. *Lithos* **2008**, *100*, 14–48. [[CrossRef](#)]
60. Kepezhinskas, P.; McDermott, F.; Defant, M.J.; Hochstaedter, A.; Drummond, M.S.; Hawkesworth, C.J.; Koloskov, A.; Maury, R.C.; Bellon, H. Trace element and Sr-Nd-Pb isotopic constraints on a three-component model of Kamchatka Arc petrogenesis. *Geochim. Cosmochim. Acta* **1997**, *61*, 577–600. [[CrossRef](#)]
61. Shervais, J.W. Ti-V plots and the petrogenesis of modern and ophiolitic lavas. *Earth Planet. Sci. Lett.* **1982**, *59*, 101–118. [[CrossRef](#)]
62. Wood, D.A.; Joron, J.L.; Treuil, M. A re-appraisal of the use of trace elements to classify and discriminate between magma series erupted in different tectonic settings. *Earth Planet. Sci. Lett.* **1979**, *45*, 326–336. [[CrossRef](#)]
63. Wang, W.; Pandit, M.K.; Zhao, J.H.; Chen, W.T.; Zheng, J.P. Slab break-off triggered lithosphere-asthenosphere interaction at a convergent margin: The Neoproterozoic bimodal magmatism in NW India. *Lithos* **2018**, *296–299*, 281–296. [[CrossRef](#)]
64. Ellam, R.M. Lithospheric thickness as a control on basalt geochemistry. *Geology* **1992**, *20*, 153–156. [[CrossRef](#)]
65. Aldanmaz, E.; Pearce, J.A.; Thirlwall, M.F.; Mitchell, J.G. Petrogenetic evolution of late Cenozoic, post-collision volcanism in western Anatolia, Turkey. *J. Volcanol. Geotherm. Res.* **2000**, *102*, 67–95. [[CrossRef](#)]
66. Green, N.L. Influence of slab thermal structure on basalt source regions and melting conditions: REE and HFSE constraints from the Garibaldi volcanic belt, northern Cascadia subduction system. *Lithos* **2006**, *87*, 23–49. [[CrossRef](#)]
67. Irving, A.J.; Frey, F.A. Distribution of trace elements between garnet megacrysts and host volcanic liquids of kimberlitic to rhyolitic composition. *Geochim. Cosmochim. Acta* **1978**, *42*, 771–787. [[CrossRef](#)]
68. Xue, Y.X.; Zhu, Y.F. Zircon SHRIMP chronology and geochemistry of the Haladala gabbro in south-western Tianshan Mountains. *Acta Petrol. Sin.* **2009**, *25*, 1353–1363, (In Chinese with English Abstract).
69. Johnson, K. Experimental cpx/and garnet/melt partitioning of REE and other trace elements at high pressures: Petrogenetic implications. *Mineral. Mag.* **1993**, *58*, 454–455. [[CrossRef](#)]
70. McKenzie, D.; O’Nions, R. Partial melt distributions from inversion of rare earth element concentrations. *J. Petrol.* **1991**, *32*, 1021–1091. [[CrossRef](#)]
71. Jung, C.; Jung, S.; Hoffer, E.; Berndt, J. Petrogenesis of Tertiary Mafic Alkaline Magmas in the Hocheifel, Germany. *J. Petrol.* **2006**, *47*, 1637–1671. [[CrossRef](#)]
72. Tang, G.J.; Chung, S.L.; Wang, Q.; Wyman, D.A.; Dan, W.; Chen, H.Y.; Zhao, Z.H. Petrogenesis of a Late Carboniferous mafic dike–granitoid association in the western Tianshan: Response to the geodynamics of oceanic subduction. *Lithos* **2014**, *202–203*, 85–99. [[CrossRef](#)]
73. Houseman, G.A.; McKenzie, D.P.; Molnar, P. Convective instability of a thickened boundary layer and its relevance for the thermal evolution of continental convergent belts. *J. Geophys. Res. Solid Earth* **1981**, *86*, 6115–6132. [[CrossRef](#)]
74. Gardien, V.; Lardeaux, J.M.; Ledru, P.; Allemand, P.; Guillot, S. Metamorphism during late orogenic extension; insights from the French Variscan belt. *Bull. De La Société Géologique De Fr.* **1997**, *168*, 271–286.
75. Davies, J.H.; von Blanckenburg, F. Slab breakoff: A model of lithosphere detachment and its test in the magmatism and deformation of collisional orogens. *Earth Planet. Sci. Lett.* **1995**, *129*, 85–102. [[CrossRef](#)]
76. Shu, L.S.; Zhu, W.B.; Wang, B.; Faure, M.; Charvet, J.; Cluzel, D. The post-collision intracontinental rifting and olistostrome on the southern slope of Bogda Mountains, Xinjiang. *Acta Petrol. Sin.* **2005**, *21*, 25–36, (In Chinese with English Abstract).
77. Wang, C.S.; Gu, L.X.; Zhang, Z.Z.; Wu, C.Z.; Tang, J.H.; Tang, X.Q. Petrogenesis and geological implications of the Permian high-k calc-alkaline granites in Harlik Mountains of eastern Tianshan, NW China. *Acta Petrol. Sin.* **2009**, *25*, 1499–1511. (In Chinese with English Abstract)
78. Wang, C.S.; Gu, L.X.; Zhang, Z.Z.; Wu, C.Z.; Tang, J.H.; San, J.Z.; Li, G.R.; Li, Z.H. Petrogenesis and tectonic implications of the Permian alkaline granite and quartz syenite assemblage in Harlik Mountains, Xinjiang. *Acta Petrol. Sin.* **2009**, *25*, 3182–3196, (In Chinese with English Abstract).
79. Wang, Q.; Zhao, G.C.; Han, Y.G.; Yao, J.L.; Liu, Q.; Guo, Y.; Zhao, Y.; Zhang, H. Late Paleozoic tectonic transition in East Junggar, NW China: Insights from I- and A-type granitic magmatism in the Karamaili region. *Lithos* **2021**, *404*, 106481. [[CrossRef](#)]
80. Laurent-Charvet, S.; Charvet, J.; Moni’e, P.; Shu, L.S. Late Paleozoic strike-slip shear zones in eastern central Asia (NW China): New structural and geochronological data. *Tectonics* **2003**, *22*, 1099–1101. [[CrossRef](#)]
81. Xiao, W.J.; Han, C.M.; Yuan, C.; Chen, H.L.; Sun, M.; Lin, S.F.; Li, Z.L.; Mao, Q.G.; Zhang, J.E.; Sun, S.; et al. Unique Carboniferous-Permian tectonic-metallogenic framework of Northern Xinjiang (NW China): Constraints for the tectonics of the southern Paleasian Domain. *Acta Petrol. Sin.* **2006**, *22*, 1362–1376, (In Chinese with English Abstract).
82. Ferrari, L. Slab detachment control on mafic volcanic pulse and mantle heterogeneity in central Mexico. *Geology* **2004**, *32*, 77–80. [[CrossRef](#)]
83. Harris, R. Geodynamic patterns of ophiolites and marginal basins in the Indonesian and New Guinea regions. *Geol. Soc. Lond. Spec. Publ.* **2003**, *218*, 481–505. [[CrossRef](#)]
84. Prelević, D.; Akal, C.; Romer, R.L.; Mertz-Kraus, R.; Helvacı, C. Magmatic response to slab tearing: Constraints from the Afyon Alkaline Volcanic Complex, Western Turkey. *J. Petrol.* **2015**, *56*, 527–562. [[CrossRef](#)]
85. Ludwig, K.R. *ISOPLLOT 3.0: A geochronological Toolkit for Microsoft Excel*; Berkeley Geochronology Center; Special Publication, No. 4.; Geochronology Center Special Publication: Berkley, CA, USA, 2003.

86. Liu, Y.; Liu, X.M.; Hu, Z.C.; Diwu, C.R.; Yuan, H.L.; Gao, S. Evaluation of accuracy and long-term stability of determination of 37 trace elements in geological samples by ICP-MS. *Acta Petrol. Sin.* **2007**, *23*, 1203–1210. (In Chinese with English abstract)
87. Chu, Z.Y.; Chen, F.K.; Yang, Y.H.; Guo, J.H. Precise determination of Sm, Nd concentrations and Nd isotopic compositions at the nanogram level in geological samples by thermal ionization mass spectrometry. *J. Anal. At. Spectrom.* **2009**, *24*, 1534–1544.

Disclaimer/Publisher's Note: The statements, opinions and data contained in all publications are solely those of the individual author(s) and contributor(s) and not of MDPI and/or the editor(s). MDPI and/or the editor(s) disclaim responsibility for any injury to people or property resulting from any ideas, methods, instructions or products referred to in the content.